metals

MDPI

Article

On the Intergranular Corrosion Properties of Thin Ferritic Stainless Steel Sheets Welded by Fiber-Laser

Niklas Sommer *, Igor Kryukov, Christian Wolf, Michael Wiegand, Martin Kahlmeyer and Stefan Böhm

Department for Cutting and Joining Manufacturing Processes, Institute for Production Technologies and Logistics, University of Kassel, Kurt-Wolters-Straße 3, 34125 Kassel, Germany; i.kryukov@uni-kassel.de (I.K.); c.wolf@uni-kassel.de (C.W.); uk021907@student.uni-kassel.de (M.W.); m.kahlmeyer@uni-kassel.de (M.K.); s.boehm@uni-kassel.de (S.B.)

* Correspondence: n.sommer@uni-kassel.de

Received: 19 June 2020; Accepted: 8 August 2020; Published: 12 August 2020

Abstract: In the present investigation, thin sheets of stabilized and unstabilized ferritic stainless steel were welded in butt joint configuration using irradiation of a 1070 nm fiber-laser. Using optical microscopy, the microstructural evolution upon alternating heat input was characterized. In addition to that, hardness and tensile tests were carried out on the specimens. Detailed focus was given to the intergranular corrosion properties, which were investigated on basis of the Strauss test with different times of exposure to the corrosive environment. Following these tests, the mechanical properties of the joints were characterized using tensile tests. A combination of the latter with an inspection by μ-CT analysis allows for the proposition of an intergranular corrosion rate with regard to the degradation of the joint strength.

Keywords: intergranular corrosion; ferritic stainless steel; laser welding; microstructure; mechanical properties; stabilization; fiber-laser; thin sheets; butt joint

1. Introduction

Ferritic stainless steels (FSS) are known for their good resistance to stress corrosion cracking (SCC) in chloride environments [1] and resistance to high-temperature oxidization [2]. Thus, FSS are used in a variety of technical applications, such as part of household appliances, parts in the petrochemical industry and equipment for chemical processing [3]. To render the construction of assembly groups possible that are in line with the demands of the specific application, it is necessary to joint FSS. A state-of-the-art joint technique for stainless steels is fusion welding, which does, however, exhibit drawbacks upon the processing of FSS. Firstly, weldments of FSS are prone to grain coarsening and the formation of grain boundary martensite, which both significantly reduce joint ductility [4,5]. Moreover, FSS are susceptible to the precipiation of chromium-rich $M_{23}C_6$ carbides at grain boundaries in the heat-affected zone (HAZ) while cooling during the thermal cycle of the welding procedure [4,6]. The aforementioned carbide precipitation leads to chromium depletion of the adjacent matrix, as cooling from a high temperature is too rapid to allow for the back-diffusion of chromium from the interior of the grains to areas alongside the grain boundaries [4–7]. As a result, this region does not provide enough chromium to enable a full passivation of the material, which is referred to as sensitization, and the joint is susceptible to intergranular corrosion (IGC) [4–7]. The described model for sensitization in stainless steels is called chromium-depletion theory and is the most accepted theory [3,6]. As IGC may lead to the failure of a joint whose surface is without further indications of damage, it is considered a catastrophic type of attack [6].

Different approaches can be taken to counter the problem of IGC in FSS. Firstly, it is possible to carry out a post-weld heat treatment (PWHT) to re-enable the solution of $M_{23}C_6$ carbides in the matrix and prevent another subsequent precipitation of the latter [5,8]. This does, nonetheless, come at the cost of a possible shape distortion due to rapid cooling rates, scaling and increased process time, which make a PWHT unattractive for large-scale industrial applications [6]. Moreover, it may not be carried out on large, structural components, thereby further inhibiting its applications [6].

Another approach is to reduce the carbon and nitrogen contents below the solubility limit so that a precipitation of carbides is fully prevented. Dilthey [5] specified the solubility limit for carbon in FSS to be around 0.01% and for carbon and nitrogen to be around 0.015%. Such FSS are subsequently referred to as super-ferrites or extra low interstitials (ELI) and show excellent resistance to intergranular corrosion [5,9].

In addition to the procedures presented above, a so-called stabilization of FSS can be carried out to increase the intergranular corrosion resistance [5,10]. The stabilization comprises of the addition of Ti or Nb to preferentially react with C and N in FSS, so that the formation of chromium-rich carbides, and thus, sensitization is inhibited [10]. Kim et al. [11] recently published new findings with regard to the intergranular corrosion mechanism of Ti-stabilized FSS. They reported that an increase of Cr content in Ti-stabilized FSS would lead to an improved resistance to IGC [11]. IGC was nonetheless induced to the samples through the segregation of un-reacted Cr around the precipitation of intergranular TiC, thereby forming a Cr-depleted matrix adjacent to the grain boundaries regardless of the Cr content [11,12]. Du Toit and Naudé [7] evaluated the sensitization behavior of Ti-stabilized FSS with 11–12% Cr using gas tungsten arc welding (GTAW) with heat inputs below approximately 0.5 $kJ \cdot mm^{-1}$ and stated that Ti-stabilization was ineffective and—depending on the chemical composition of the steel—might even be detrimental to IGC resistance, as the rapid cooling rates during the high-temperature thermal cycle of welding inhibited the precipitation of TiC but nonetheless allowed the precipitation of CrC during the low-temperature cooling regime. Moreover, in the high-temperature heat-affected zone (HT-HAZ) close to the melt pool, TiC was dissolved and retained in solid solution to room temperature for that it acted as a ferrite-forming element. As a result, they postulated that a reduction of heat input below 0.2 $kJ \cdot mm^{-1}$ could prevent the dissolution of TiC in the HT-HAZ and thus improve the sensitization behavior. This thesis was disproved by Weigl [13] who investigated the mechanical and corrosive properties of austenitic and ferritic stainless steel mixed welds. The results revealed that, despite the application of low heat inputs due to the utilization of a continuous wave (cw) disk-laser, a sensitization of the FSS could not be prevented. Moreover, it was deduced from the results that the microstructure and grain coarsening in the weld seam were dominant factors for the sensitization of FSS. The corrosive properties, which were evaluated using the salt spray test in a temperature regime slightly above ambient temperature, were nonetheless improved through a stabilization with Ti [13].

Taskin et al. [14] also published results of austenitic and ferritic stainless steel mixed welds, joined by CO_2-laser, and reported grain coarsening in the seam of the AISI 430 joint partner. In addition to the aforementioned studies, Evin et al. [15] also investigated butt joint welds of AISI 430 joined by fiber-laser and reported significant grain growth in the fusion zone with martensite in the interdendritic space and a subsequent reduction in deformation work and toughness. The use of a pulsed Nd:YAG-laser also allowed for significant grain growth in the fusion zone of AISI 430 welded in lap-joint configuration, as was shown by Mostaan and Nematzadeh [16]. With regard to Ti-stabilized FSS, Lakshminarayanan and Balasubramanian [17] used irradiation of a CO_2-laser to weld sheets of 11 wt.% Cr AISI 409M in butt joint configuration. They reported a higher hardness and tensile strength of the weld metal as compared to the base material, but drastically reduced grain growth in the HAZ and weld seam, which was attributed to the rapid solidification during laser welding. Moreover, they reported an insignificant increase of weld metal impact toughness when compared to the base material.

From the different studies mentioned above, it is evident that welding of FSS—especially laser welding—comprises complex metallurgical processes, which directly affect their corrosive properties.

Yet, a thorough investigation of the intergranular corrosion properties of laser-welded FSS in a high-temperature regime and sulfuric acid environment has not been published to the best of the authors' knowledge. The presented study thus investigated the microstructural features obtained by welding of thin FSS sheets using a fiber-laser and characterized their IGC properties using the Strauss test. Moreover, as IGC may cause sudden and severe failure of FSS joints, a time-dependent IGC-rate based on the deterioration of joint strength was identified, rather than one based on the loss of mass or spatial advancement.

2. Materials and Methods

2.1. Stainless Steel Sheets

The size of the stainless steel sheets used for the welding experiments was $150 \times 100 \times 0.8\,mm^3$ with a cold-rolled and bright-annealed surface condition. The two materials investigated were the unstabilized FSS EN X6Cr17 (1.4016, AISI 430) and the Ti-stabilized FSS EN X3CrTi17 (1.4510, AISI 430Ti). The nominal and actual chemical compositions of the sheet materials are found in Table 1.

Table 1. Nominal and actual chemical compositions of the (a) AISI 430 and (b) AISI 430Ti sheet materials used in the investigation. Nominal chemical composition derived from [18].

(a)	**Chemical Composition [wt.%]**						
	Fe	C	N	Cr	Ti	Ni	Mo
nominal	bal.	0.08	0.04	16.00	0.00	0.00	0.00
actual	bal.	0.041	0.142	16.18	0.001	0.156	0.046
(b)	**Chemical Composition [wt.%]**						
	Fe	C	N	Cr	Ti	Ni	Mo
nominal	bal.	0.05	0.04	16.00	0.80	0.00	0.00
actual	bal.	0.018	0.079	16.18	0.326	0.260	0.046

2.2. Laser Welding

To provide for a repeatable welding result of thin sheet material in butt joint configuration, the selected sheets had to be securely fastened using a custom clamping device, whose setup can be seen in Figure 1.

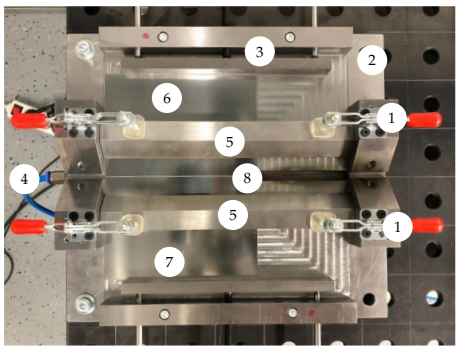

1	holding-down clamps
2	base
3	counter-holder
4	gas backing
5	pressure pads
6	sheet no.1
7	sheet no.2
8	joint area

Figure 1. Clamping device used for the welding experiments.

Using two pressure pads in form of bars and four holding-down-clamps, which enabled a uniform load transmission, the sheets were firmly pressed onto the base of the device. Moreover, the butt-edges

were held in place by two adjustable counterholders which also inhibited any movement of the joint area due to thermal expansion during the thermal cycle of welding.

As the beam source, a 1070 nm, 2 kW fiber-laser (YLS-2000-S2, IPG Laser GmbH, Burbach, Germany) with a top-hat intensity profile was used and the beam was guided to the focusing optics (MWO44, Reis Lasertec GmbH, Würselen, Germany) using a process fiber with a diameter of 100 µm. The beam was focused onto the sheet surface, yielding a beam diameter of approximately 200 µm.

To prevent oxidization of the weld seam and seam root during the thermal cycle, argon shielding gas (purity $\geq$ 99.996%) with a flow rate of 30 L·min^{-1} was employed.

Since the results of preliminary investigations indicated successful welding results at energy inputs of around 20 J·mm^{-1}, as can be seen in the results of Lisiecki et al. [19], who used a disk-laser to weld zinc-coated steel sheets of the same thickness and joint configuration, an experimental design with four different energy inputs was used in the present investigation, as can be seen in Table 2.

Table 2. Experimental design and parameters for each of the investigated materials.

Sample	Traverse Speed	Laser Power	Welding Energy Input
	[mm·s^{-1}]	[W]	[J·mm^{-1}]
1	40	720	18
2	40	800	20
3	40	880	22
4	40	960	24

2.3. Microstructural Characterization and Mechanical Testing

Following the laser welding of the joint partners, samples were extracted from the welds for each distinct investigation, as shown in Figure 2.

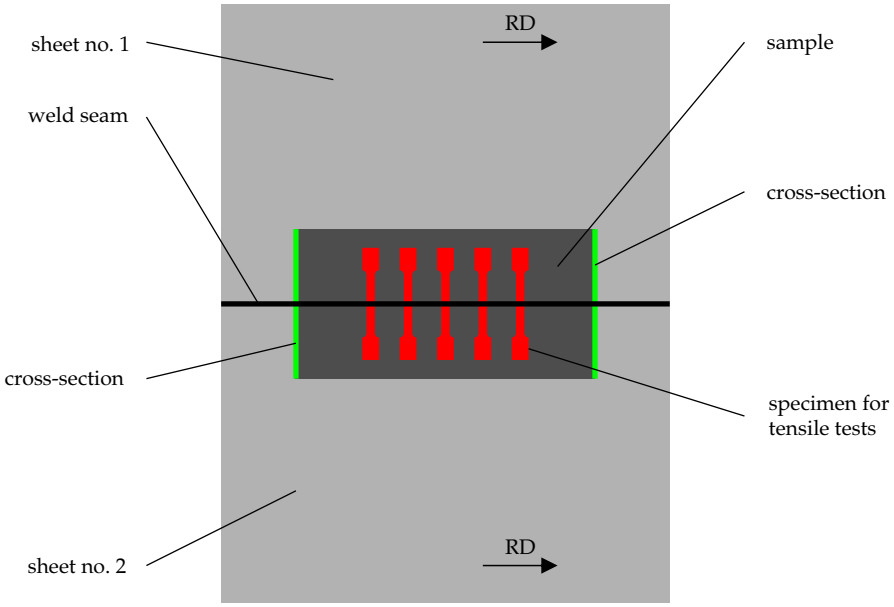

Figure 2. Schematic illustration of sample extraction, and locations of cross-sections and specimens for tensile testing with rolling direction (RD) of the sheet material.

Using a band-saw, metal shears and a wet separating grinder, the sheet material was cut into samples of 100 × 40 × 0.8 mm^3 for further mechanical and corrosion testing. A total of three samples was produced for each set of parameters. For each of the samples, the weld seam quality and microstructure were investigated using polished and etched cross-sections. The etchant comprised approximately 47.15% HCl, 47.15% H_2O, 4.7% HNO_3 and 1% pickling inhibitor. Prior to the corrosion

tests, five specimens for tensile tests were cut out of one welded sample of a distinct energy input using electric discharge machining (EDM) and used as the weld-reference, while the other samples were prepared for the corrosion tests detailed in Section 2.4. Following the corrosion tests, five specimens for tensile tests were extracted from the corroded samples in order to evaluate the mechanical properties after the corrosive attack. The polished and etched cross-sections were investigated using optical microscopy (DM2600, Leica Microsystems GmbH, Wetzlar, Germany), allowing for a characterization of the microstructure before and after the corrosion tests. In addition to that, micro-hardness measurements were carried out using the weld cross-sections obtained beforehand and via utilization of an automated hardness-testing machine (KB30, KB Prüftechnik GmbH, Hochdorf-Assenheim, Germany). Micro computer-tomography (μ-CT, Xradia Versa 520, Carl Zeiss AG, Oberkochen, Germany) was used for a three-dimensional characterization of intergranular attack and fracture shape. The tensile specimens, whose geometry is depicted in Figure 3, were tested on a tensile-testing machine (Z100, ZwieckRoell AG, Ulm, Germany) in accordance with DIN EN ISO 6892-1 [20] with a strain rate $\dot{\varepsilon}$ of 0.0067 s^{-1}.

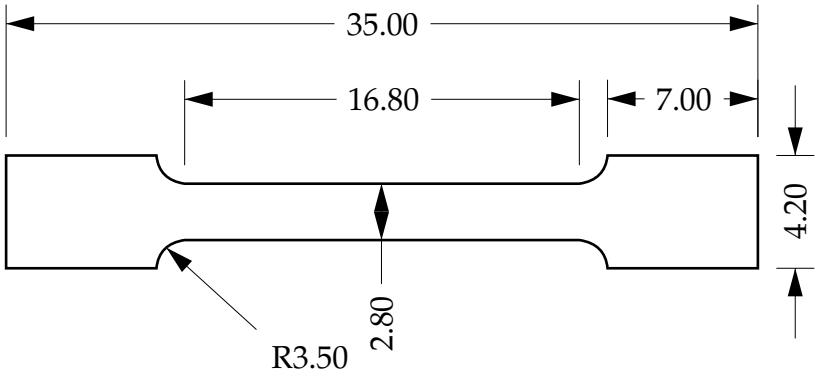

Figure 3. Technical drawing of the specimens used in tensile testing, lengths in mm. Scaled from type H geometry of [21].

2.4. Corrosion Testing

The corrosion tests were conducted on the basis of DIN EN ISO 3651-2 (Strauss test) [22]. Prior to the tests, the surfaces of the samples (dimensions 100 × 40 × 0.8 mm^3) were ground down to 180 grit size using silicon carbide (SiC) paper. The samples were contacted with copper chips on the bottom of the glass flask and immersed in a boiling solution of 138 g H_2SO_4 (ρ_{20} = 1.84 g·mL^{-1}) and 75 g $CuSO_4 \cdot 5\,H_2O$ dissolved in desalinated water to a total solution volume of 750 mL. The samples were then exposed to the corrosive environment for a duration of 10 and 20 h, respectively. This allowed for a temporally-resolved characterization of IGC. Two samples of one type of FSS were tested simultaneously in a glass flask. A schematic representation of the setup for IGC testing can be seen in Figure 4.

Since the cross-sectional area of the edges of each sample also comprised a sensitized weld seam and HAZ, which did result in an uneven intergranular attack in preliminary investigations, the edges of the samples were embedded in an unfilled, cold-curing epoxy-resin (EP660, Polytec PT GmbH, Karlsbad, Germany). Subsequently, the epoxy-resin on the edges was cold-cured for a duration of 16 h. Hence, an uneven intergranular attack from the edges could be excluded.

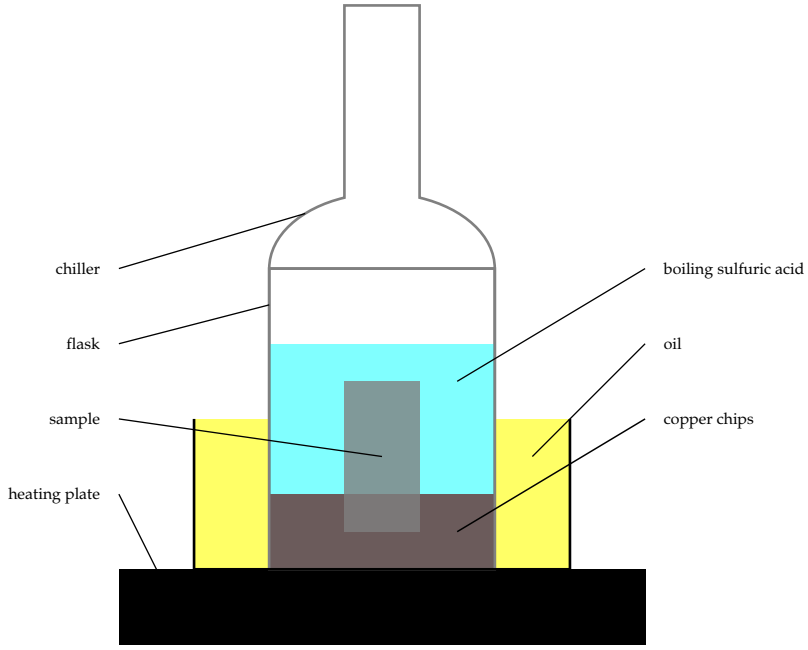

Figure 4. Schematic representation of the setup used for IGC testing of FSS.

3. Results and Discussion

3.1. Weld Seam Characterization and Hardness Testing

The macrostructures of the weld seams obtained for AISI 430 are depicted in Figure 5. As can be derived from the etched macrographs, the clamping device enabled a reproducible fixation of the thin sheet material with almost no linear offset. For all shown cross-sections, the weld seams exhibited minimal undercutting at the upper surface of the unstabilized FSS regardless of the welding energy input employed. The weld roots, on the other hand, indicated the influence of energy input to their respective shapes, as incursions of the root were decreased with energy inputs of 22 J·mm^{-1} and 24 J·mm^{-1}.

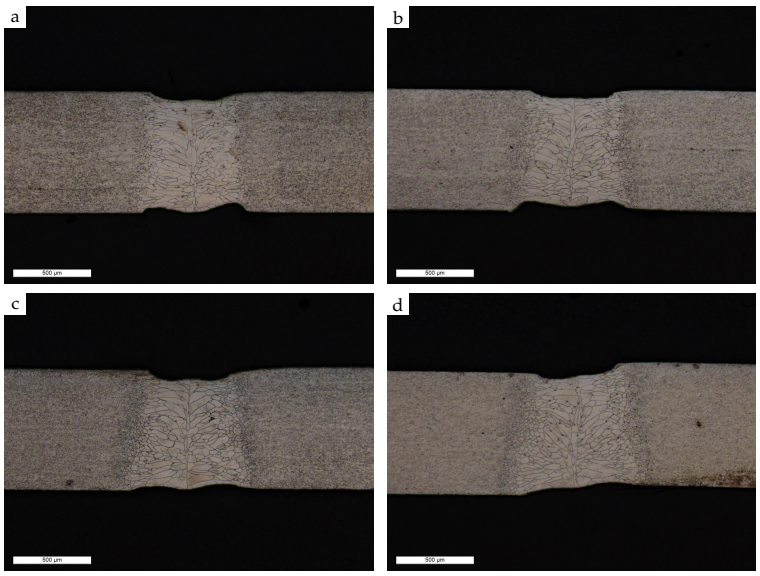

Figure 5. Etched macrographs of AISI 430 weld seams obtained at energy inputs of (**a**) 18 J·mm^{-1}, (**b**) 20 J·mm^{-1}, (**c**) 22 J·mm^{-1} and (**d**) 24 J·mm^{-1}.

Impartial from the energy input, however, grain coarsening could be observed within the fusion zone, as was expected from the results of Evin et al. [15]. Through comparisons with the results of the authors mentioned beforehand, it became evident that the grain growth in the present investigation was not as prominent, which may be attributed to the different energy inputs used, yet the alternating energy inputs in the present investigation yielded different widths of weld seam and HAZ. The narrowest weld seam and HAZ could be observed with energy inputs of 18 J·mm^{-1}, while a minimal increase of both widths was to be perceived with increasing energy input. Even at an energy input of 24 J·mm^{-1} though, the difference in weld seam and HAZ width might be described as minimal.

The microstructural evolution upon alternating energy input differed insignificantly, as is shown in Figure 6. For the lowest energy input of 18 J·mm^{-1}, the formation of grain boundary martensite could be identified. At an energy input of 24 J·mm^{-1}, in comparison, the formation of martensite was somewhat reduced. This effect can be explained by the increased heat input of the latter, and thus, a decrease of cooling rate which is essential to the formation of martensite. Moreover, the area of transition from the weld seam to HAZ, and subsequently base material, was larger for an energy input of 24 J·mm^{-1} than for an input of 18 J·mm^{-1} which can be attributed to the correspondingly increased heat input as well. The observations of microstructural evolution agree with the findings of Pekkarinen and Kujanpää [23], who compared keyhole and conduction laser welding of AISI 430 to GTAW welding.

Etching of micrographs also revealed strongly contrasting grain boundaries, which suggests a different chemical reaction of the etchant with the grain boundary, and therefore a different chemical composition of the latter, which supports the theory of significant carbide precipitation at the grain boundaries, as one would expect from an unstabilized FSS. This hypothesis was further supported by the quantities of interstitial C and N found in the actual chemical composition of AISI 430.

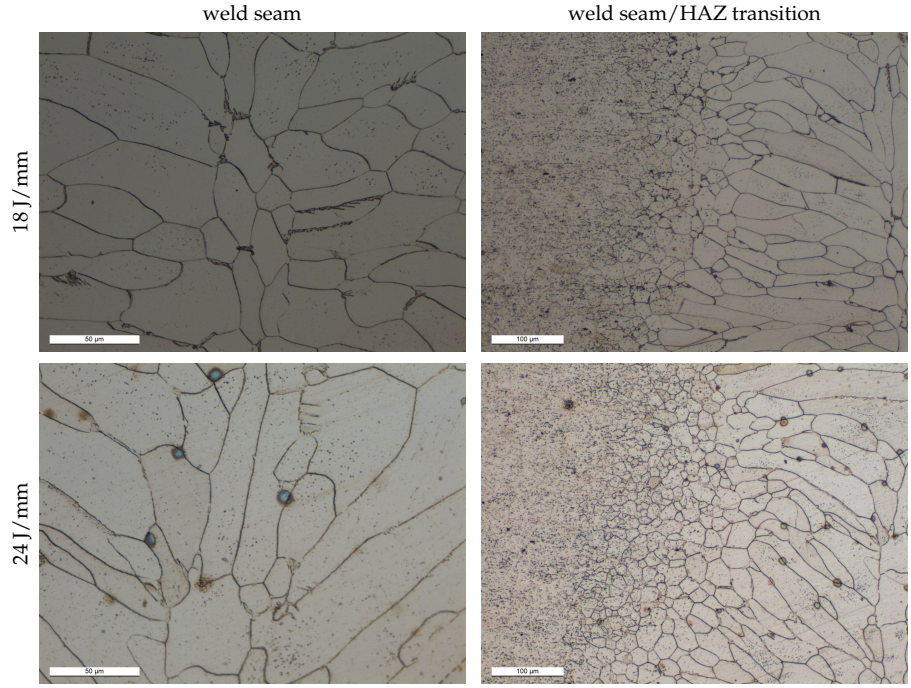

Figure 6. Etched micrographs of AISI 430 weld seams obtained at energy inputs of 18 J·mm^{-1} and 24 J·mm^{-1}. Some sample preparation artifacts are visible.

As shown in Figure 7, the etched macrographs of AISI 430Ti indicated reproducible clamping as well. For lower energy inputs of 18 J·mm^{-1} and 20 J·mm^{-1}, pronounced incursion of the seam root could be observed which was alleviated by an increase of energy input and its subsequent influence

on melt pool dynamics. Moreover, more distinctive grain coarsening than in AISI 430 was identified within the fusion zone. This fact could be ascribed to the role of Ti as a strong ferrite-forming element. Due to the rapid solidification of laser welding, some Ti was retained in solid solution down to room temperature, and thus promoted the formation of large ferrite grains, as was proposed for low heat input welding by Du Toit and Naudé [7]. This was further supported by the microstructural investigation of AISI 430Ti welds depicted in Figure 8.

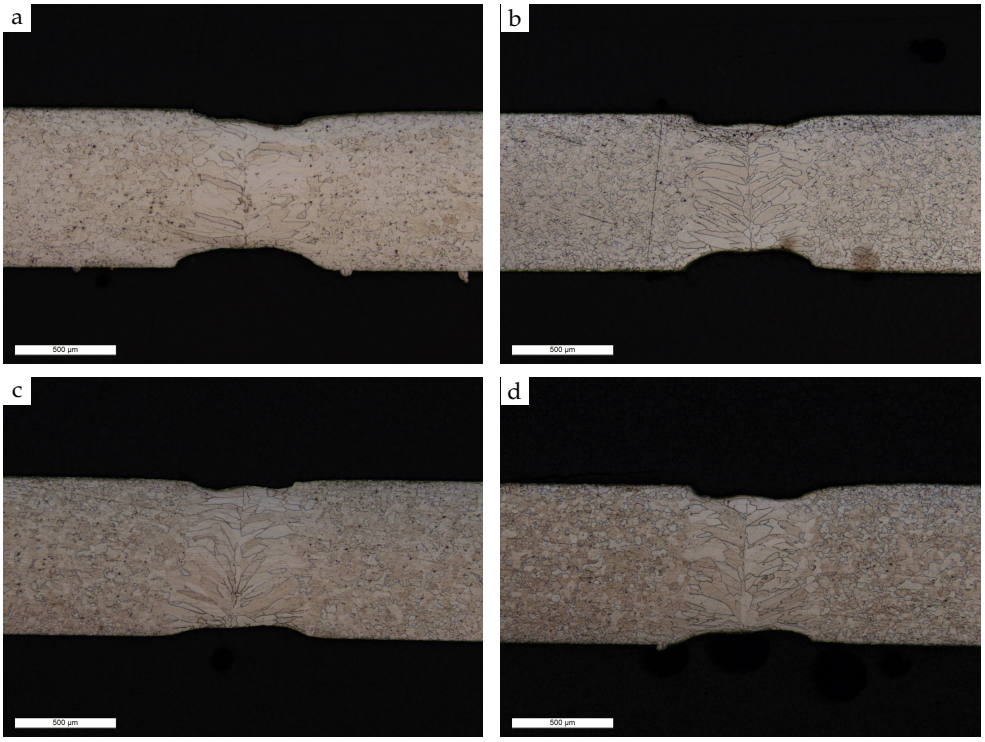

Figure 7. Etched macrographs of AISI 430Ti weld seams obtained at energy inputs of (**a**) 18 J·mm^{-1}, (**b**) 20 J·mm^{-1}, (**c**) 22 J·mm^{-1} and (**d**) 24 J·mm^{-1}.

Whereas a large number of rectangular TiC precipitations could be observed in the base material, only a very limited number of these rectangular TiC precipitates were to be found within the weld seam, and some could be identified within the HAZ. This supports the theory that very low heat input welding processes, such as laser welding, might effectively hinder the precipitation of stabilizing carbides such as TiC to a certain degree in the first, rapid cooling segments following solidification. Yet, through the contrasting grain boundaries of the etched micrographs, as were to be seen with AISI 430, the authors propose that the precipitation of some very fine carbides occurred. For once, these precipitates were found in the border area of weld seam and HAZ, but more dominantly, they were to be found within the weld seam itself, which resulted in strongly contrasting grain boundaries, as can be seen in Figure 8. For this reason, it was concluded that ferrite-forming Ti in solid solution enabled a fully ferritic solidification with a body-centered cubic lattice (bcc), in which, on the other hand, less carbon was soluble as compared to a face-centered cubic lattice (fcc). As a result, the bcc lattice in the weld seam was supersaturated in carbon, and thus induced carbide precipitation at the grain boundaries of the weld seam. The exact chemical composition of the carbides could not be determined, but it was assumed that both TiC and $M_{23}C_6$ were precipitated at the grain boundaries during the corresponding thermal cycle of laser welding. These observations are in agreement with those postulated by Bäumel [24], who identified that the behavior for GTAW of 17 wt.% Cr FSS with Ti-stabilized 17 wt.% Cr FSS as filler material.

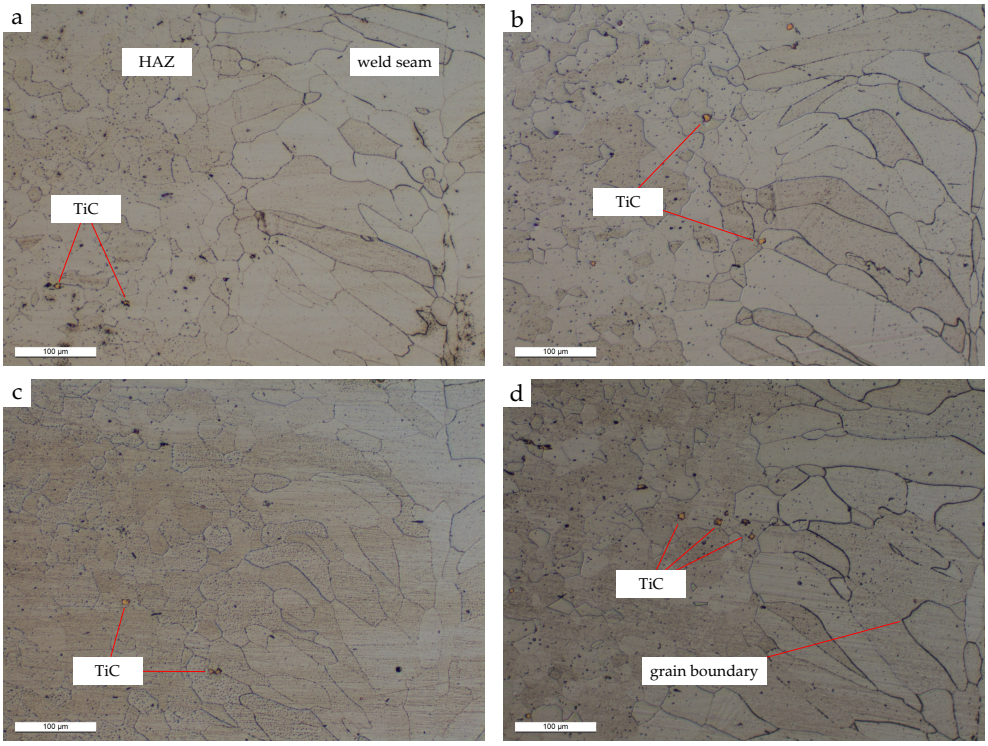

Figure 8. Etched micrographs of AISI 430Ti weld seams and adjacent HAZ, obtained at energy inputs of (**a**) 18 J·mm^{-1}, (**b**) 20 J·mm^{-1}, (**c**) 22 J·mm^{-1} and (**d**) 24 J·mm^{-1}.

The obtained results of the hardness measurements using the method of Vickers are shown in Figure 9. As was expected from the microstructural evolution in the presented weldments of AISI 430, rapid cooling rates and the subsequent formation of grain boundary martensite contributed to an increase in hardness in the weld seam and in the adjacent HAZ. Alternating the energy input, on the other hand, neither yielded significant nor systematic hardness changes. For all measurements of AISI 430, the hardness increase could be localized in a rather narrow region of 600 µm to each side of the weld centerline, from where the hardness steadily decreased through the HAZ to reach the level of the base material.

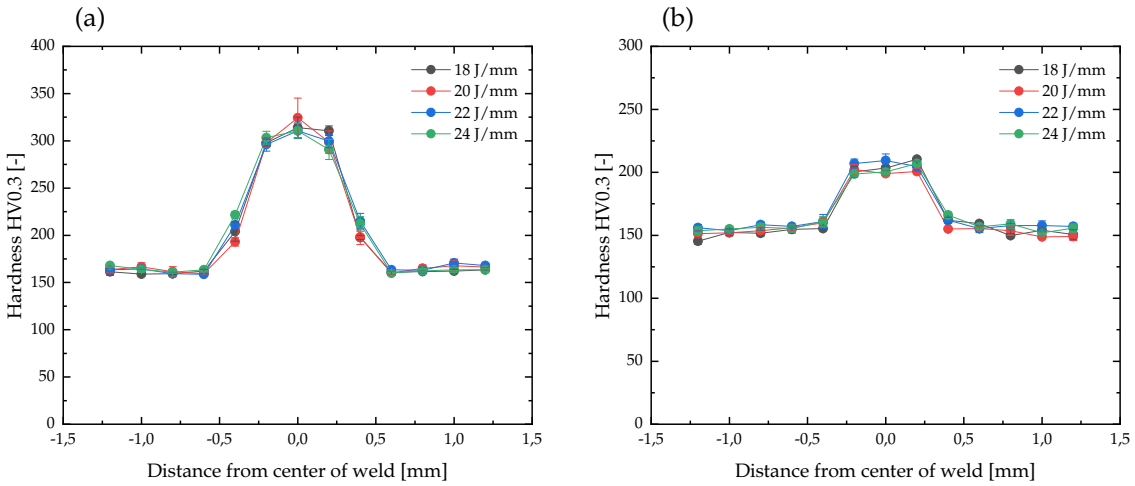

Figure 9. Hardness measurements of (**a**) AISI 430 and (**b**) AISI 430Ti welded at varying energy inputs. Mean values and standard error of the mean (SEM) calculated from three different measurements.

Measurements across the weld seam and HAZ of AISI 430Ti also indicated an increase in hardness, which was, nonetheless, not as prominent as the one observed in AISI 430. From the weld centerline, which exhibited a hardness of around 200 to 210 HV, the hardness gradually decreased through the adjacent regions to reach values of the base material approximately 400 µm from each side of the weld centerline. The identified difference with AISI 430 can be ascribed to the lower overall carbon content of the material as well as the presence of Ti as alloying element, which enabled a fully ferritic solidification without the formation of grain boundary martensite. Within the energy input regime investigated in the paper at hand, no systematic influence of energy input on hardness could be detected. It was to be concluded that a slim weld seam and HAZ were obtained through the utilization of a fiber-laser with a spot diameter of 200 µm for both investigated materials, despite the fact that the region of hardness increase was smaller in AISI 430Ti.

3.2. Mechanical Properties in Welded Condition

Despite the different macroscopic characteristics of the weld seams, the joints of each respective material exhibited similar mechanical properties. Firstly, for AISI 430, no distinct variation of the ultimate tensile strength (UTS) could be perceived for varying energy inputs, as can be seen in Figure 10. Moreover, it was to be observed that the elongation at break (EAB) only exhibited negligible variations upon a change of energy input. A similar behavior was identified for the specimens of AISI 430Ti, which did not reveal any distinct changes in UTS or EAB with regard to energy input.

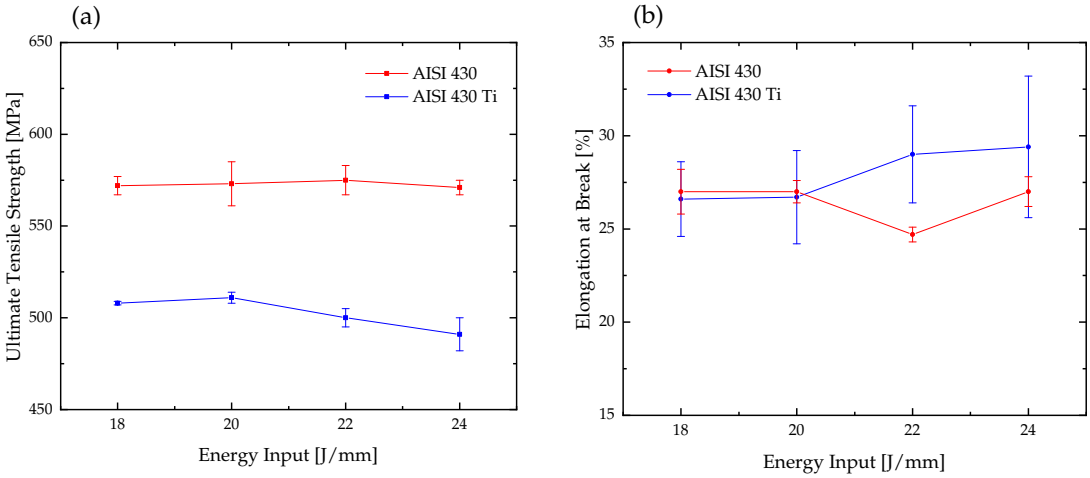

Figure 10. Comparison of (**a**) ultimate tensile strength and (**b**) elongation at break for both materials investigated, welded at different energy inputs. Mean values and SEM calculated from five tensile tests.

For a comparison, specimens for tensile testing were extracted from the un-welded, cold-rolled base material perpendicular to the rolling direction (RD) and tested as specified in Section 2.3. The unstabilized FSS AISI 430 exhibited an increase of UTS by 5.09% to 572.75 MPa in its welded condition when compared to the base material at 545 MPa, as shown in Figure 11. The EAB, on the other hand, was reduced by 18.44% from 32.4% to 26.43%, which can be attributed to the microstructural evolution upon welding and subsequent grain coarsening within the fusion zone. Nevertheless, cracking was only observed in the base material of the tensile specimens rather than in the weld seam, as can be seen in Figure 12. These results do, however, not concur with those published by Evin et al. [15] who reported a drastic reduction in EAB for laser-welded AISI 430 to 6.0%. Despite the reduction in EAB for welded condition in the present investigation, the ductility of the joint obtained was superior to that published by Evin et al. [15]. The aforementioned authors employed a laser power of 2100 W at a traverse speed of 70 mm·s^{-1}, yielding an energy input of 30 J·mm^{-1}. When comparing these results to the ones presented in the investigation at hand with regard to the microstructural

evolution, it is evident that the reduced heat input in the present investigation resulted in a finer microstructure than that presented by Evin et al. [15]. Hence, it is to be derived from these observations that the finer microstructure and somewhat limited, but not completely suppressed grain coarsening significantly contributed to an improvement of ductility for the joints presented. In addition to that, only limited amounts of martensite were formed at the grain boundaries.

As for AISI 430Ti, the UTS was decreased by 2.62% from 516 MPa to 502.5 MPa in welded condition, while the EAB was reduced by 21.78% from 35.7% to 27.93%. Since the solidification of AISI 430Ti is fully ferritic, the formation of grain boundary martensite could not be identified as the reason for a reduction in joint ductility. In this case, it was rather attributed to grain coarsening within the fusion zone, which could not be suppressed despite the utilization of very low energy inputs. Ti acted as a strong ferrite forming element and furthered the susceptibility to grain coarsening of the weld seam, as presented in the preceding Section 3.1, resulting in larger grains within the fusion zone than those observed in AISI 430. In contrast to AISI 430, cracking was also only identified in the weld seam during tensile testing except for two specimens welded at a heat input of 22 J·mm^{-1}, which exhibited failure in the base material. Yet, from the fractography images in Figure 12, it is evident that the weld seam exhibited comparatively high levels of ductility during tensile testing as pronounced necking of the aforementioned could be observed, rather than brittle failure.

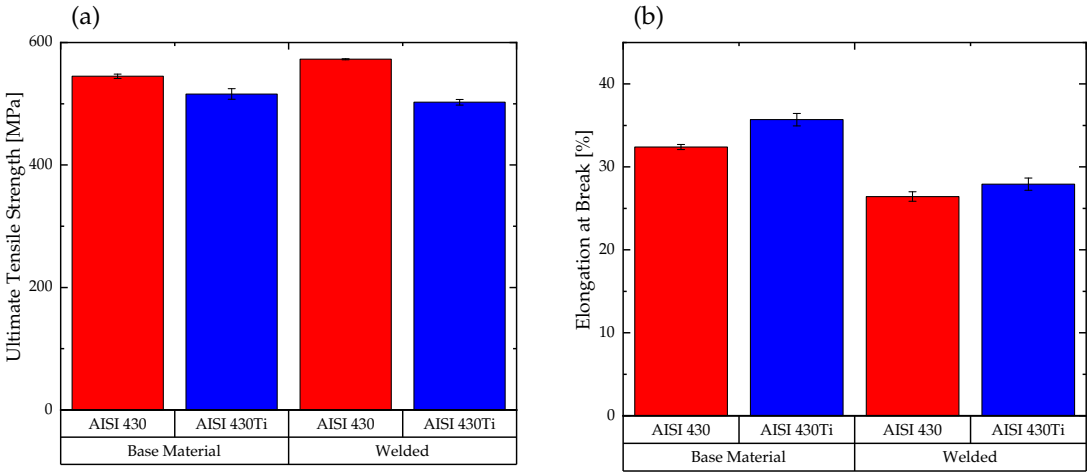

Figure 11. Comparison of (**a**) ultimate tensile strength and (**b**) elongation at break for both materials in as-received and welded condition. Mean values and SEM for welded condition calculated from the results obtained for different energy inputs.

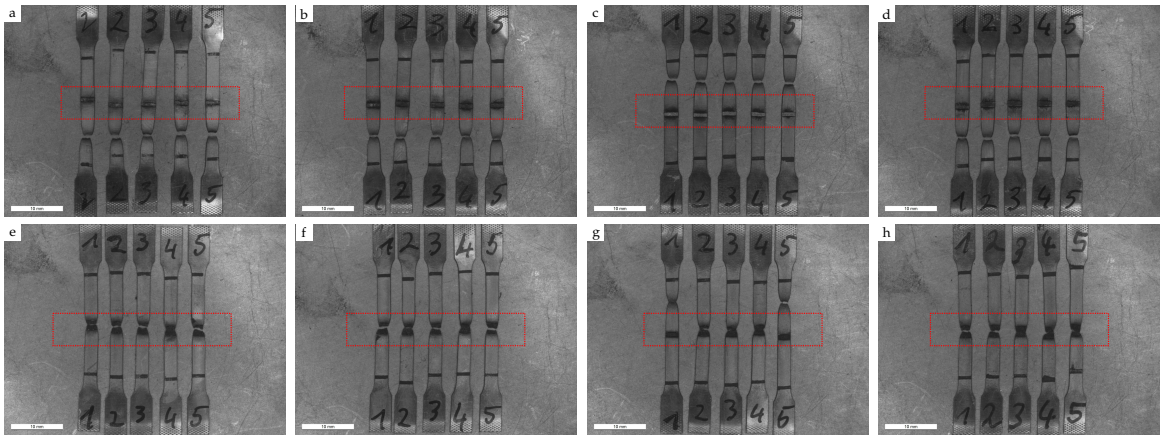

Figure 12. Photographic images of fractures in tensile specimens of (**a**–**d**) AISI 430 and (**e**–**h**) AISI 430Ti welded at different energy inputs (left to right: 18 J·mm^{-1}–24 J·mm^{-1}). Weld seam area marked with red rectangles.

3.3. Intergranular Corrosion and Impact on Tensile Properties

The design of specimen extraction from the corroded samples facilitated the characterization of tensile properties following the exposure to the corrosive environment for a distinct time. However, it was observed that tensile testing was only possible for specimens of Ti-stabilized AISI 430Ti, as all samples of AISI 430 exhibited joint failure without loading—regardless of the exposure time to the corrosive environment and energy input employed during welding. Thus, it was evident that the characterization of IGC propagation in these samples could only be described using cross-sections, which are to be found in Figure 13. They revealed the propagation of IGC along the HAZ adjacent to the weld seam which ultimately led to the disconnection of the weld seam from the HAZ and sheet material. Moreover, intergranular attack was also visible within the weld seam itself, as entire grains were dislocated from the weld metal. The grain boundaries within the weld seam were also observed in strong contrast to the grains themselves in the un-etched cross-sections, and thus they strengthened the hypothesis of a corrosive attack within the weld seam. This theory was further supported by the cross-sections obtained after an exposure of 20 h, presented in Figure 13, and concurs with the mechanism described by Kaesche [25]. Obviously, the corrosion mechanism itself was not only limited to the formation of slim, sensitized ditches adjacent to the grain boundaries. Rather, with increasing exposure time, the edges of the sensitized ditches were not passivated, hence allowing the corrosive attack to widen and establish grooves with localized "pitting corrosion."

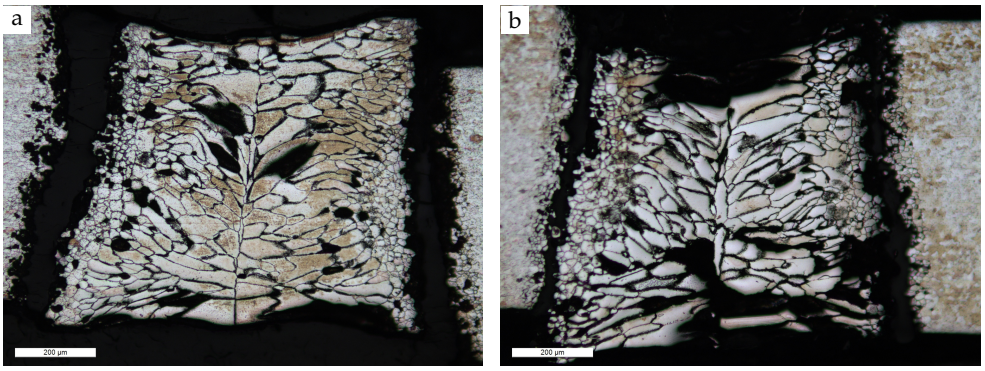

Figure 13. Etched cross-section of AISI 430 after (**a**) 10 h and (**b**) 20 h of exposure to the corrosive environment. Weld produced at an energy input of 24 $J \cdot mm^{-1}$.

From these results, it was concluded that the utilization of low-energy input laser welding could not effectively retard the precipitation of $M_{23}C_6$ carbides in unstabilized FSS, and therefore not prevent the sensitization of the material. Furthermore, it was evident that the rather harsh corrosive environment of boiling H_2SO_4 + $CuSO_4 \cdot 5\,H_2O$ solution led to a rapid failure of unstabilized FSS, so a finer temporal resolution is required to characterize the tensile properties following a corrosive attack.

The corroded samples of AISI 430Ti, on the other hand, did not exhibit failure without loading so that a detailed and temporally resolved characterization of their tensile properties was rendered possible. As it is presented in Figure 14, the results of tensile testing after 10 and 20 h of exposure to the corrosive environment did not indicate a systematic influence of energy input on the tensile properties following a corrosive attack. Rather, the results at hand foreshadowed a localized attack within weld seam of the Ti-stabilized FSS, as specimens from a singular sample revealed deviations of their tensile properties. This was further supported by the cross-sections obtained from the samples. While certain cross-sections did exhibit significant intergranular attack, others indicated only minimal propagation of IGC, as is shown in Figure 15. Hence, the theory of a localized intergranular attack within this Ti-stabilized FSS was furthered. This supported the theory of Kim et al. [11,12] that sensitization of Ti-stabilized FSS occurred due to the segregation of unreacted Cr around fine TiC precipitates at the grain boundary. Since a large number of—presumably TiC and $M_{23}C_6$—precipitates were found within the weld seam during the microstructural characterization described in the preceding subsection,

IGC seemed to be propagated along the precipitations at the grain boundaries, hence inducing grooves that acted as nuclei for cracking during tensile testing. Moreover, IGC was not only propagated along the vertical grain boundaries and its resulting grooves, but also spread horizontally, which indicated a localized "pitting corrosion," as was observed in AISI 430 due to lack of passivation.

Apart from these observations, it was perceived that the UTS and EAB both decreased due to IGC. Thus, it was concluded that Ti-stabilization had a positive influence on the IGC resistance of laser-welded AISI 430Ti when compared to AISI 430. Yet, it could not hinder IGC propagation in this type of FSS.

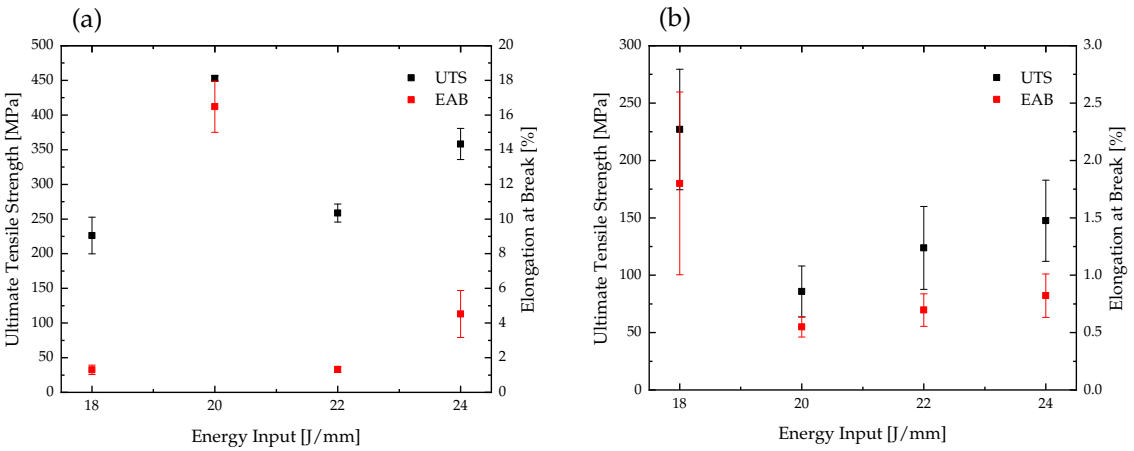

Figure 14. Mean values and SEM of ultimate tensile strength and elongation at break for AISI 430Ti after (**a**) 10 h and (**b**) 20 h of exposure to the corrosive environment, calculated from five tensile tests.

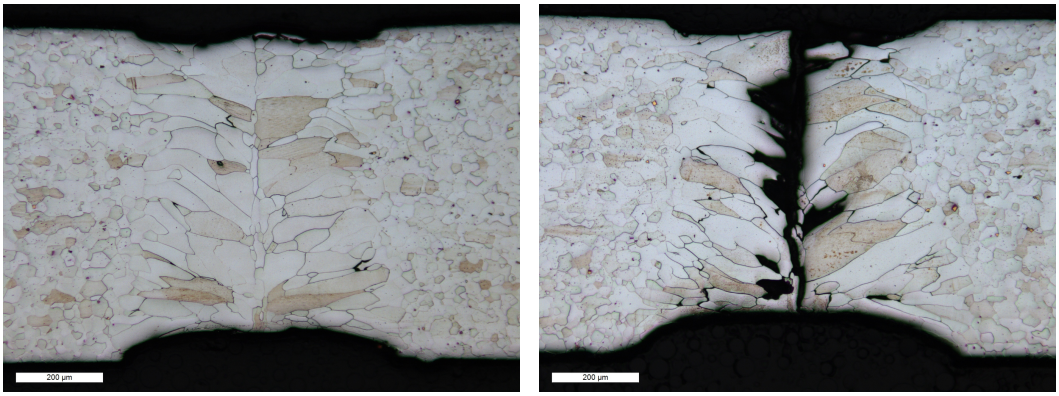

Figure 15. Etched cross-sections of AISI 430Ti after exposure to the corrosive environment for 20 h, both welded at an energy input of 20 J·mm^{-1} and extracted from a single weld seam.

The mean value of UTS in welded AISI 430Ti was reduced by 35.53% to 323.95 MPa with an exposure of 10 h to the corrosive environment, as can be derived from Figure 16. A total exposure of 20 h led to a further reduction of UTS to 146.01 MPa, thereby yielding an almost linear degradation of UTS with increasing exposure time. As for EAB, the mean value was reduced by 78.85% to 5.91% following a corrosive attack with a duration of 10 h. After an exposure of 20 h, the EAB was diminished to 0.97%, so that the degradation of EAB exhibited characteristics of an exponential decline. Since the cross-sections of Ti-stabilized FSS revealed strongly differing microstructural evolutions upon corrosive attack, the utilization of tensile tests appeared to be suitable for characterization of IGC severity in joints of laser-welded FSS.

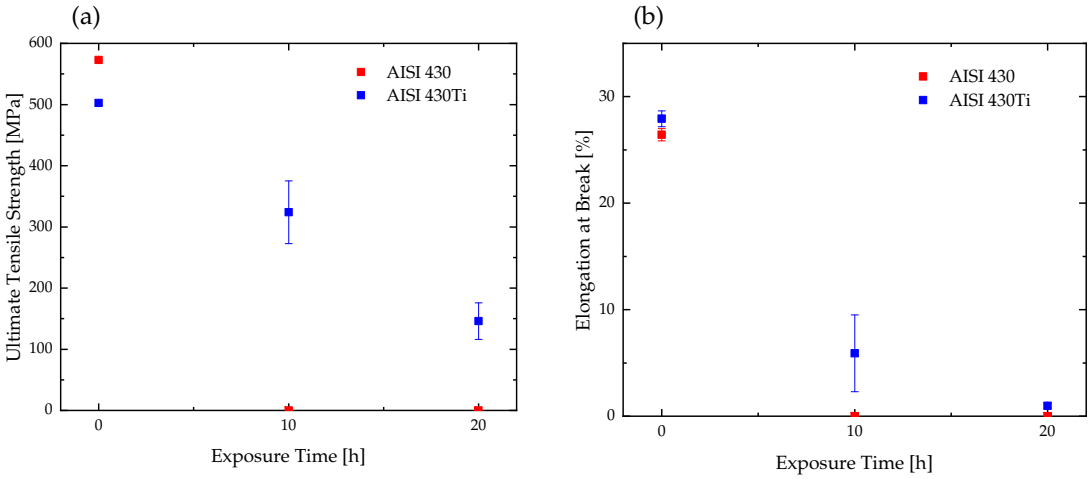

Figure 16. Mean values and SEM of (**a**) ultimate tensile strength and (**b**) elongation at break for AISI 430 and AISI 430Ti as a function of exposure time to the corrosive environment, calculated from the results obtained at different energy inputs.

Moreover, whereas the failure in the welded and uncorroded specimens of AISI 430Ti occurred within the weld seam or base material in a ductile manner (Figures 11 and 12), the mode of failure became rather brittle with an increasing exposure to the corrosive environment (Figure 16) and failure then only occurred in the weld seam. This fact was further investigated through μ-CT analysis of the fracture surfaces, depicted in Figure 17.

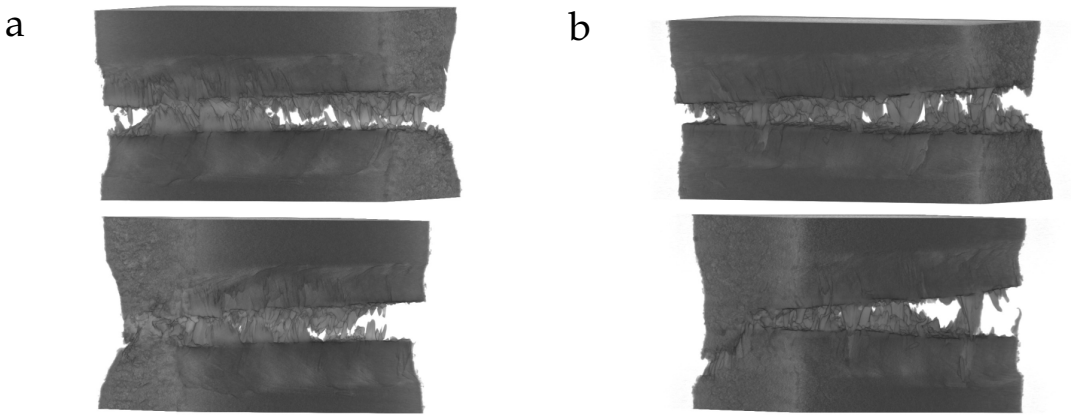

Figure 17. 3D rendering of fracture in AISI 430Ti after (**a**) 10 h and (**b**) 20 h exposure to the corrosive environment, obtained by μ-CT analysis. Top images: front view, bottom images: rear view.

From these results, it was evident that upon exposure to the acidic environment, necking during tensile testing was almost completely suppressed, further proving the mode of failure after IGC as rapid and cataclysmic, even in Ti-stabilized FSS. In addition to that, μ-CT analysis revealed the propagation of intergranular cracking in the center of the weld seam, as shown in Figure 18; for that it was concluded that in the Ti-stabilized FSS examined in the investigation at hand, carbide precipitation within the weld seam was responsible for IGC, and subsequently, crack propagation. As a result, it was deduced from the results that after an exposure time of 10 h, corrosion was not propagated so far as to enable an instant failure of the joint. Rather, non-corroded regions acted as anchors during tensile testing. As corrosion was further propagated through the weld seam after an exposure time of 20 h, these regions were diminished and therefore enabled a more brittle failure of the joint.

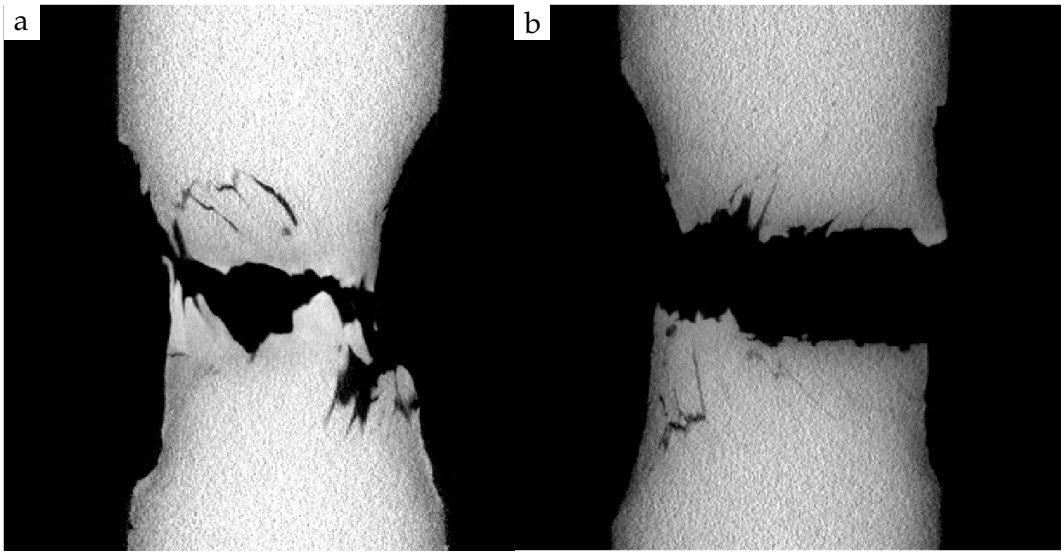

Figure 18. Fractography images from within the weld seam of AISI 430Ti after (**a**) 10 h and (**b**) 20 h exposure to the corrosive environment, obtained by μ-CT analysis.

4. Conclusions

In the investigation at hand, thin sheets of unstabilized and Ti-stabilized FSS were welded in butt-joint configuration using irradiation of a 1070 nm fiber-laser. The conducted microscopic imaging, tensile testing and corrosion analysis allow for a number of conclusions to be deduced from the results presented beforehand:

- Despite the utilization of low energy input laser welding, grain coarsening within the weld seam and HAZ could not be prevented in AISI 430 and AISI 430Ti.
- Upon etching, strongly contrasting grain boundaries were observed in cross-sections of the welds.
- In AISI 430, $M_{23}C_6$ carbide precipitation could not be prevented despite very low energy input.
- In cross-sections of AISI 430Ti, square-sized TiC from the base material could only be found in limited numbers within the weld seam, for which the authors propose that some TiC was retained in solid solution upon cooling through the thermal cycle of welding, and the Ti acted as a ferrite forming element while very fine TiC and $M_{23}C_6$ were precipitated along grain boundaries.
- Regardless of the microstructural evolution during welding, both materials exhibited excellent tensile properties with only limited reductions in ductility when compared to the base material.
- After corrosive attack, AISI 430 failed without further loading along the HAZ; hence, a finer temporal resolution is needed to provide for the proposition of a corrosion rate based on the degradation of joint strength.
- Following the exposure to the acidic, corrosive environment, AISI 430Ti revealed decreasing tensile properties with increasing exposure time.
- Tensile specimens of AISI 430Ti exhibited failure within the weld seam, rather than in the HAZ; for that it was concluded that sensitized grain boundaries within the weld seam were responsible for IGC propagation.
- At low energy inputs employed during laser welding, a systematic variation of energy input did not result in a significant difference in IGC resistance.
- Upon corrosive attack, the mode of failure was changed from a rather ductile to brittle failure, which was attributed to the propagation of IGC within the weld seam of AISI 430Ti.
- It was possible to define the corrosion rate as temporally resolved degradation of joint strength.

Author Contributions: Conceptualization, N.S.; methodology, N.S. and M.K.; validation, N.S., I.K., C.W. and M.K.; formal analysis, N.S.; investigation, N.S. and M.W.; resources, N.S., I.K. and M.K.; data curation, N.S.; writing—original draft preparation, N.S.; writing—review and editing, N.S., I.K., C.W., M.W., M.K. and S.B.; visualization, N.S.; supervision, N.S. and S.B.; project administration, N.S.; funding acquisition, S.B. All authors have read and agreed to the published version of the manuscript.

Funding: The shown results were achieved in the project "Kombiniertes in-situ Laserstrahl-/Laserstrahlauftragschweißen bei nichtrostenden Stählen zum Schutz vor interkristalliner Korrosion" (reference IGF 20.129N), which is supervised by the Forschungsvereinigung Schweißen und verwandte Verfahren e.V. of the German Welding Society and funded by the German Federation of Industrial Research Associations (AiF) by means of the Federal Ministry of Economic Affairs and Energy (BMWi) on the basis of a decision by the German Bundestag.

Acknowledgments: The authors would like to thank Miele and Cie. KG (Gütersloh, Germany), in particular, Alix Gaspard and Robert Austermann, for providing the materials used in the present study and the analysis of their actual chemical compositions. In addition to that, the authors would like to express their gratitude to Christian Staab, who helped to carry out the corrosion experiments, and Michael Hübner, who extracted the specimens from the welded samples.

Conflicts of Interest: The authors declare no conflict of interest. The funders had no role in the design of the study; in the collection, analyses or interpretation of data; in the writing of the manuscript, or in the decision to publish the results.

Abbreviations

The following abbreviations are used in this manuscript:

AISI	American Institute of Iron and Steel
ASS	austenitic stainless steel
bcc	body-centered cubic
C	carbon
CO_2	carbon dioxide
Cr	chromium
CrC	chromium carbide
$CuSO_4$	copper sulfate pentahydrate
cw	continuous wave
ELI	extra low interstitials
EN	European Norm
fcc	face-centered cubic
Fe	iron
FSS	ferritic stainless steel
GTAW	gas tungsten arc welding
HCl	hydrochloric acid
HNO_3	nitric acid
H_2O	water
H_2SO_4	sulfuric acid
HAZ	heat-affected zone
HT-HAZ	high-temperature heat-affected zone
IGC	intergranular corrosion
Mo	molybdenum
N	nitrogen
Nb	niobium
Nd:YAG	neodymium yttrium-aluminum-garnet
PWHT	post-weld heat treatment
RD	rolling direction
SCC	stress corrosion cracking
SEM	standard error of the mean
SiC	silicon carbide
Ti	titanium
TiC	titanium carbide
UTS	ultimate tensile strength

References

1. Newberg, R.T.; Uhlig, H.H. Stress Corrosion Cracking of 18% Cr Ferritic Stainless Steels. *J. Electrochem. Soc.* **1972**, *119*, 981. [CrossRef]
2. Sabioni, A.C.S.; Huntz, A.M.; Luz, E.C.D.; Mantel, M.; Haut, C. Comparative study of high temperature oxidation behaviour in AISI 304 and AISI 439 stainless steels. *Mater. Res.* **2003**, *6*, 179–185. [CrossRef]
3. Amuda, M.O.H.; Mridha, S. An Overview of Sensitization Dynamics in Ferritic Stainless Steel Welds. *Int. J. Corros.* **2011**, *2011*, 1–9. [CrossRef]
4. Folkhard, E.; Rabensteiner, G.; Perteneder, E.; Schabereiter, H.; Tösch, J. *Metallurgie der Schweißung Nichtrostender Stähle*; Springer: Vienna, Austria, 1984; doi:10.1007/978-3-7091-4449-7. [CrossRef]
5. Dilthey, U. *Schweißtechnische Fertigungsverfahren 2: Verhalten der Werkstoffe beim Schweißen*; Auflage, B., Ed.; Springer: Berlin/Heidelberg, Germany, 2005. [CrossRef]
6. Čihal, V. Intergranular Corrosion of Steels and Alloys. In *Materials Science Monographs*; Elsevier: Amsterdam, The Netherlands, 1984; Volume 18.
7. Du Toit, M.; Naudé, J. The influence of stabilization with titanium on the heat-affected zone sensitization of 11 to 12% chromium ferritic stainless steels under low heat input welding conditions. *Weld World* **2011**, *55*, 38–47, doi:10.1007/BF03321285. [CrossRef]
8. Schulze, G. *Die Metallurgie des Schweissens: Eisenwerkstoffe—Nichteisenmetallische Werkstoffe*; Aufl, N.B., Ed.; VDI-Buch, Springer: Heidelberg, Germany, 2010.
9. Kiesheyer, H.; Lennartz, G.; Brandis, H. Korrosionsverhalten hochchromhaltiger, ferritischer, chemisch beständiger Stähle. *Mater. Corros. Korros.* **1976**, *27*, 416–424. [CrossRef]
10. Huang, X.z.; Wang, D.; Yang, Y.t. Effect of Precipitation on Intergranular Corrosion Resistance of 430 Ferritic Stainless Steel. *J. Iron Steel Res. Int.* **2015**, *22*, 1062–1068. [CrossRef]
11. Kim, J.K.; Kim, Y.H.; Lee, J.S.; Kim, K.Y. Effect of chromium content on intergranular corrosion and precipitation of Ti-stabilized ferritic stainless steels. *Corros. Sci.* **2010**, *52*, 1847–1852. [CrossRef]
12. Kim, J.K.; Kim, Y.H.; Lee, B.H.; Kim, K.Y. New findings on intergranular corrosion mechanism of stabilized stainless steels. *Electrochim. Acta* **2011**, *56*, 1701–1710. [CrossRef]
13. Weigl, M. *Laserstrahlschweißen von Mischverbindungen aus Austenitischen und Ferritischen Korrosionsbeständigen Stahlwerkstoffen*; Bericht aus dem Lehrstuhl für Photonische Technologien; Meisenbach: Bamberg, Germany, 2014; Volume 254.
14. Taskin, M.; Caligulu, U.; Kolukisa, S. The Effect of Welding Speed on the Laser Welding of AISI 430 Ferritic Stainless–AISI 1010 Low-Carbon Steel. *Pract. Metallogr.* **2009**, *46*, 598–608. [CrossRef]
15. Evin, E.; Tomáš, M.; Výrostek, M. Laser-Beam Welding Impact on the Deformation Properties of Stainless Steels When Used for Automotive Applications. *Acta Mech. Autom.* **2016**, *10*, 189–194. [CrossRef]
16. Mostaan, H.; Nematzadeh, F. Micro Laser Welding of AISI 430 Ferritic Stainless Steel: Mechanical Properties, Magnetic Characterization and Texture Evolution. *Int. J.* **2017**, *14*, 1–8.
17. Lakshminarayanan, A.K.; Balasubramanian, V. Evaluation of Microstructure and Mechanical Properties of Laser Beam Welded AISI 409M Grade Ferritic Stainless Steel. *J. Iron Steel Res. Int.* **2012**, *19*, 72–78. [CrossRef]
18. Deutsches Institut für Normung e. V. *Nichtrostende Stähle—Teil 2: Technische Lieferbedingungen für Blech und Band aus Korrosionsbeständigen Stählen für Allgemeine Verwendung: Deutsche Fassung (DIN EN 10088-2)*; Beuth Verlag GmbH: Berlin, Germany, 2014.
19. Lisiecki, A.; Burdzik, R.; Siwiec, G.; Warczek, J.; Folęga, P.; Oleksiak, B. Disk Laser Welding of Car Body Zinc Coated Steel Sheets/Spawanie Laserem Dyskowym Blach Ze Stali Karoseryjnej Ocynkowanej. *Arch. Metall. Mater.* **2015**, *60*, 2913–2922. [CrossRef]
20. Deutsches Institut für Normung e. V. *Metallische Werkstoffe-Zugversuch—Teil 1: Prüfverfahren bei Raumtemperatur (ISO/FDIS 6892-1:2019)*; German and English Version prEN ISO 6892-1:2019; Beuth Verlag GmbH: Berlin, Germany, 2019.
21. Deutsches Institut für Normung e. V. *Prüfung Metallischer Werkstoffe—Zugproben: DIN 50125:2016-12*; Beuth Verlag GmbH: Berlin, Germany, 2016.
22. Deutsches Institut für Normung e. V. *Ermittlung der Beständigkeit Nichtrostender Stähle Gegen Interkristalline Korrosion—Teil 2: Nichtrostende Austenitische und Ferritisch-Austenitische (Duplex)-Stähle*; Korrosionsversuch in Schwefelsäurehaltigen Medien (ISO 3651-2:1998): Deutsche Fassung EN ISO 3651-2:1998; Beuth Verlag GmbH: Berlin, Germany, 1998.

23. Pekkarinen, J.; Kujanpää, V. The effects of laser welding parameters on the microstructure of ferritic and duplex stainless steels welds. *Phys. Procedia* **2010**, *5*, 517–523. [CrossRef]
24. Bäumel, A. Selektive Korrosion an Verbindungsschweißen von Stählen. *Mater. Corros. Korros.* **1966**, *17*, 299–307, doi:10.1002/maco.19660170404. [CrossRef]
25. Kaesche, H. *Die Korrosion der Metalle: Physikalisch-Chemische Prinzipien und Aktuelle Probleme*, 3rd ed.; Klassiker der Technik; Springer: Berlin/Heidelberg, Germany, 2011.